RSC Applied Interfaces

Accepted Manuscript

This article can be cited before page numbers have been issued, to do this please use: P. Singh, S. Agrawal, D. Khare, V. Tiwari and A. K. Dubey, *RSC Appl. Interfaces*, 2025, DOI: 10.1039/D5LF00045A.

ROYAL SOCIETY OF CHEMISTRY

rsc.li/RSCApplInter

View Article Online
DOI: 10.1039/D5LF00045A

Interfacial response of Mg-Ca-Si-Zr Nanoparticles for Transformative Orthopedic Therapeutics

Priya Singh[a], Somesh Agrawal[b], Deepak Khare[a], Vinod Tiwari[b] and Ashutosh Kumar Dubey [a,] *

[a] Department of Ceramic Engineering, Indian Institute of Technology (BHU) Varanasi - 221005, India.

[b] Department of Pharmaceutical Engineering and Technology, Indian Institute of Technology (BHU) Varanasi, 221005, India.

Abstract

The debris particles, discharged due to the degradation and wear, initiate an inflammatory response at the implantation site or lead to the aseptic loosening of the prosthesis, ultimately resulting in implant failure over time. The toxicity concern becomes more severe for the release of nano-sized debris particles due to augmented interfacial interactions, even if the bulk counterpart is highly biocompatible. Towards this perspective, the present study aims to assess the *in vivo toxicity* both, local and systemic of $Mg_{1-x}Ca_xSi_{1-x}Zr_xO_3$ (x = 0 - 0.4) [MCSZO-X, X = 0 - 4] nanoparticles using rat model. Initially, the *in vitro* cytotoxicity of varying concentrations (0.25, 2.5, and 25 mg/ml) of MCSZO-X nanoparticles was evaluated using MG-63 cells. The cell proliferation increases after the early interfacial interactions. Following this, 100 µl of MCSZO nanoparticles (25 mg/ml) was administered through intra-articular injection into the knee joint of male Wistar rats. The biochemical analyses showed no pathological change in the liver and kidney of the injected group of rats. Also, the histopathological analyses demonstrated that there is no inflammation due to interfacial interactions with injected nanoparticles in various organs like liver, heart, kidney and knee. Overall, the above findings pave the way for further advancement in bone repair and implant design.

Keywords: *$MgSiO_3$, silicate, inflammation, in vivo, biochemical assay orthopedic implant, histopathological analyses.*

* Correspondence: akdubey.cer@iitbhu.ac.in (A. K. Dubey); # +918726823415

View Article Online
DOI: 10.1039/D5LF00045A

1. Introduction

The wear resistance of implants and the biological response of debris particles are the key factors in determining the long-term success of implants.[1] The debris particles, released due to degradation, friction, and wear, have the ability to trigger harmful biological reactions at the implantation sites due to interfacial interactions, resulting in periprosthetic osteolysis, inflammation, and aseptic loosening.[1, 2] Specifically, inflammation activates osteoclast cells, leading to the improper balance between osteoclasts and osteoblasts. This imbalance initiates osteolysis, ultimately causing aseptic loosening of the prosthetic implant.[1-3] Also, the properties of debris particles, such as their composition, morphology, volume, and size, play a crucial role in their biological response and profoundly affect the fate of peri-implant cells.[4] Numerous studies (both, *in vitro* and *in vivo*) demonstrated that nanoparticles consistently raise interfacial concerns because of their specific features, such as surface area, morphology, size and concentration.[5, 6] The wear particles, smaller than 2 μm, can be easily entered to other organs, penetrate inside the cell through plasma membrane and induce toxicity, even at sub-cellular level.[7, 8] Wang et al.[8] revealed that intra-articular injection (with concentrations of 2 and 20 mg/ml) of TiO_2 nanoparticles (38 to 54 nm) into the knees of rats, allowed the migration of TiO_2 nanoparticles into crucial organs like heart and liver and results in pathological damage to these organs. Additionally, biochemical assessments demonstrated impairments in the renal and hepatic systems of the rats.[8] Mabrouk et al.[9] reported that the performance of the liver does not affect after implantation of pure and BaO (3 and 5 %)-doped $MgSiO_3$ nanopowders in the tibia of fractured rats.

Several studies reported the excellent osteogenic activity and antibacterial efficiency, *in vitro,* of Mg and Ca silicate-based bioceramics which substantiate the potentiality of these materials for bone tissue engineering applications.[10-17] $Mg_{1-x}Ca_xSi_{1-x}Zr_xO_3$ (x = 0 - 0.4) has been

View Article Online
DOI: 10.1039/D5LF00045A

established as an excellent biomaterial, however, the toxicity of such nanoparticles due to interfacial interactions has not been explored. As a step ahead, this study examined the *in vivo* toxicity of $Mg_{1-x}Ca_xSi_{1-x}Zr_xO_3$ (x = 0-0.4) [MCSZO-X (X = 0 - 4)] nanoparticles using rat model.

Initially, MG-63 cells were exposed with different concentrations of MCSZO-X eluates (0.25, 2.5, and 25 mg/ml in normal saline) for 1 and 3 days. Following the in vitro results, the highest concentration (25 mg/ml) of MCSZO-X nanoparticle eluates were injected into the knee joints of rat for 7 days. After the designated exposure period, the rats were euthanized. Hematological evaluations were conducted to measure white blood cell (WBC) counts and mean corpuscular volume (MCV). Additionally, biochemical analyses were performed on the serum to assess the overall functional status of the organs in the groups treated with nanoparticles, including evaluations of alkaline phosphatase and creatinine activity. The histopathological evaluations were conducted to identify any potential signs of inflammation on major organs (kidney, heart and liver) and knee joint.

2. *In-vivo* toxicity assessment of MCSZO-X (X = 0 -4) nanoparticles

2.1.1. Sample preparation and material characterization

The procedure for synthesizing micron-sized MCSZO-X (X = 0 -4) powders has already been reported in our earlier work.[18] The solid-state method was employed to prepare these powders within a compositional range of X = 0 to X = 4. The particle size of prepared micron-sized powders was reduced via ball milling (Fritsch Pulverisette 5) for 12-14 h at 300 rpm. For this purpose, cylindrical zirconia balls (6 mm diameter, 6 mm height, 0.9 g/ ball) were used for grinding. The ratio of balls to powder was 10:1. In a ball mill jar, 50 g (about 56 balls) of zirconia balls were combined with 5 g of MCSZO-X (X = 0 - 4) powder in 50 ml of ethanol.

View Article Online
DOI: 10.1039/D5LF00045A

2.1.2. Phase and morphological characterization

The phase verification of MCSZO-X nanoparticles was done via X-ray diffraction with Cu Kα radiation (XRD, X-ray Diffractometer, Rigaku Miniflex II Desktop) with a wavelength of 1.5418 Å (scan range: 20 to 60° and step size: 0.02°). High-resolution scanning electron microscopy (Nova Nano SEM, FEI) was used to determine the particle size and morphology of the ball-milled MCSZO-X nanoparticles.

2.1.3. Eluate solution preparation

The MCSZO-X ball-milled particles were autoclaved at 121ºC for 25 - 30 min. Following this, the sterilized powders were dispersed in normal saline (0.9 % w/v NaCl) at three different concentrations of 0.25 (C1), 2.5 (C2), and 25 (C3) mg/ml. Saline served as the medium for injecting MCSZO-X nanoparticles into rats. To achieve uniformly in dispersed nanoparticles, the eluates were ultrasonicated for 15 min after every 6 h, over a period of 2- 4 days. Before injection, the eluates were again sterilized.

2.1.4. Leaching behavior

The leaching behavior of ready eluates (C1, C2 and C3) of MCSZO-X nanoparticles were examined in saline after 1, 3 and 5 days of incubation. ICP-AES was used to evaluate the amounts of leached ions (Mg, Ca, Si and Zr) from different elutes of MCSZO-X samples. Before measurements, the resulting solutions were diluted 10 times in distilled water, followed by filtration using a pore size of 0.22 micron-sized syringe filter.

2.1.5. Cellular response

The cellular behavior of MCSZO-X (X= 0 - 4) nanoparticles due to interfacial interactions was studied using MG-63 cells. The procured cells were grown in a CO_2 incubator under specific conditions of 37 ºC temperature, 5 % CO_2, and 95 % humidity. The DMEM (Himedia) with a growth factor of 15 % FBS (Gibco) and 1 % antibiotic (Antibiotic-Antimycotic, Gibco) solution was used as a growth media. After, 90 - 95 % confluency, the

View Article Online
DOI: 10.1039/D5LF00045A

cells were trypsinized using 0.25% trypsin (Gibco) solution and 10^4 cells/ml were seeded onto glass coverslips (gelatin-coated) in 24-well. The well plate was then incubated for a period of 12 h for the adhesion of cells to the substrate. After 12 h of the incubation period, 100 µl of eluates (C1, C2, and C3) of M1 M2, M3, M4 and M5 samples were added to the adhered cells. The cells with nanoparticles were further incubated for 1 and 3 days, respectively, to quantify the viability of cells. The proliferation of cells, grown on MCSZO-X samples, was measured using the MTT (3-(4, 5-dimethylthiazol-2-yl)-2, 5-diphenyl-tetrazolium-bromide, SRL). After cell seeding for 1 and 3 days, 500 µL of MTT reagent was added to samples. After 6 h of incubation in the prescribed environment, the well plate was taken out, and the solution was replaced with DMSO (500 µL, Himedia) to dissolve the formazan crystals. After that, the culture for each sample was moved to a 96-well plate and optical density was measured using an ELISA reader at the wavelength of 595 nm.

2.3. *In vivo* assessment

2.3.1. Animals

In this study, male Wister rats, weighing 250 ± 50 g, were used. Rats were housed under controlled conditions of humidity and temperature (21-25 ± 2ºC) with a light-dark cycle. The rats were randomly allocated to different experimental groups (n = 5/group). The animal experimentation protocols were properly authorized by the Institute Animal Ethics Committee at the Indian Institute of Technology, Banaras Hindu University, situated in Varanasi, Uttar Pradesh, India (IAEC approval number: IIT(BHU)/IAEC/2023/II/083).

2.3.2. Experimental procedure

Rats were intraarticularly administered with 100 µl of MCSZO-X nanoparticles (Fig. 1), suspended in sterile saline (25 mg/ml). Animals were divided into seven groups with n = 5 rats in each group. Group 1 was used as a control and group 2 was injected with saline. The remaining five groups, designated as M1, M2, M3, M4 and M5, were treated with MCSZO-X

View Article Online
DOI: 10.1039/D5LF00045A

nanoparticles. The animals were closely observed for any signs of physical changes during the initial 30 min, following the experimental procedures. Subsequently, they were monitored at regular intervals over the next 24 h, with particular attention given to first 4 h. Animals were daily observed for a duration of 7 days. Body weights of all the rats were measured at day 1, 3, 5 and 7 post-injections. After 7 days, blood serum was collected through retro-orbital plexus puncture. Following this, the animals were sacrificed with high dose of anesthesia and major organs (kidney, heart and liver) and knee joint were collected for histopathological studies.

2.4. Hematology and Biochemical assay

EDTA (Ethylenediaminetetraacetic acid) -coated vials were used to collect the serum samples for hematological analyses, and hematologic toxicity was assessed using an automated hematological analyzer (Cell-Dyn Ruby Hematology Analyzer). Hematological parameters like, white blood cells (WBC) and mean corpuscular volume (MCV) were estimated. Biochemical testing was performed on serum, which was obtained after the centrifugation (4000 RPM for 10 min) of blood samples, to evaluate the activities of creatinine and alkaline phosphatase (ALP) in the rats, injected with nanoparticles and compared with control and saline treated group. AUTOSPAN Liquid and MKB Alkaline Phosphatase kit was used for the determination of ALP activity. The entire test was conducted as per the guidelines, provided by the manufacturer. Additionally, creatinine level was also measured using standard kit (Crystal Chem, IL, USA).

2.5. Histopathological analyses

The fixed tissues, including the kidney, liver, and heart, were dehydrated using a series of ethanol solution. The paraffin blocks were made after fixing with paraffin wax. Hematoxylin and eosin (H&E) stains were used for staining the tissue blocks after they were divided (10 μm) for histopathological evaluations. The tissues of the fixed knee joint were first

View Article Online
DOI: 10.1039/D5LF00045A

dehydrated with ethanol solution, and then decalcification was done with nitric acid solution (10%). The paraffin-embedded joint tissue blocks were prepared for histopathological examination, similar to other organs. Nikon Eclipse LV 100 ND fluorescence microscope photographs of stained tissues have been examined.

2.6. Statistical analyses

The SPSS software was applied to investigate the statistically significant differences among various testing by means of the one-way ANOVA method and Tukey's post hoc tests at a $p \leq 0.05$. For in vivo data analyses, Graph Pad Prism software was used. The weights of animals were examined through the application of two-way ANOVA, whereas the hematological parameters were statistically assessed via one-way ANOVA (at $p > 0.05$).

3. Results and discussion

3.1. Phase analyses

Fig. 2 represents the XRD pattern of MCSZO-X (X = 0 - 4) nanoparticles. XRD pattern confirms the formation of monoclinic pure $MgSiO_3$ [JCPDS # 35-0610] phase with P21/c space group. In addition, a few minor peaks were indexed with JCPDS # 34-0189 with Pmnb space group. However, the peak shifted towards a lower angle with the incorporation of Ca/ Zr with increasing the concentration, from X = 0 to X = 3, as shown in Fig. 2 b. Moreover, the crystallite size was calculated from Scherrer's formula.[19, 20] The crystallite size reduced from 35 nm to 31 nm as the Ca/Zr increased from X = 0 to X = 3. After that crystallite size again increases from 31 nm to 33 nm with an increase in the amount of Ca / Zr, from X = 3 to X = 4.

Fig. 2 b demonstrates that with increasing the concentration from X = 0 to X = 3, the peaks shifted towards lower 2 θ values from 28.24º to 28.08º. With a further increase in the concentration from X = 0 to X = 3, the peak shifts towards the higher angle again from 28.08º to 28.33º (as represented by the enlarged view). The incorporation of larger Ca^{2+} cations

View Article Online
DOI: 10.1039/D5LF00045A

(1.34 Å) at the reduced Mg^{2+} site (0.72 Å) and Zr^{4+} cations (0.74 Å) at the diminutive Si^{4+} site (0.40 Å) leads to an expansion of the lattice in $MgSiO_3$ as the concentrations of Ca and Zr increase from 0 to 3, resulting in peak shifts toward lower 2θ values. Nonetheless, as the concentration ascends beyond 0.3, the peaks migrate to elevated angles owing to lattice contraction stemming from the presence of a greater quantity of Ca^{2+} at the Mg^{2+} locus.[11, 21-23] The five polymorphic variants of $MgSiO_3$ adopt either monoclinic or orthorhombic crystal structures.[24] As the concentration of Ca and Zr increased from 0 to 0.2, peak positions in X-ray diffraction patterns shifted to lower 2θ angles, from 22.96º to 22.82º. This shift results from the substitution of larger Ca^{2+} ions for smaller Mg^{2+} ions at the A-site and Zr^{4+} ions for smaller Si^{4+} ions at the B-site. Conversely, increasing Ca and Zr concentrations from 0.2 to 0.4 caused the peaks to shift to higher 2θ values, from 22.82º to 23.12º, likely due to lattice contraction in MCSZO-X bioceramics driven by greater Ca^{2+} substitution at Mg^{2+} sites. For compositions with x = 0.3 to x = 0.4, phase analyses revealed minor secondary phases, ZrO_2 (JCPDS # 37-1484), $CaSiO_3$ (JCPDS # 43-1460) and $CaMgSiO_4$ (JCPDS # 19-0240). The emergence of an additional secondary phase, Mg_2SiO_3, poses challenges in synthesizing single-phase $MgSiO_3$. Therefore, with increasing Ca and Zr concentrations from 0.3 to 0.4, further minor phases, including ZrO_2, $CaSiO_3$, Ca_2MgSiO_7, Mg_2SiO_4, and $CaMg(SiO_3)_2$, began to appear.

The FT-IR spectra of MCSZO-X nanoparticles confirmed the incorporation of Ca/Zr in the $MgSiO_3$ structure (Fig. 3). The specific peaks of Si - O at 470, 500, 600, and 1052 cm^{-1} correspond to bending and stretching vibrations, respectively. The bending vibration observed at around 800 cm^{-1} in Si-O-Si indicates the formation of $MgSiO_3$.[25, 26] Moreover, the vibrational peak, representing Si-O within silicate tetrahedra, is found at 682 cm^{-1}.

View Article Online
DOI: 10.1039/D5LF00045A

Furthermore, the stretching and bending vibrations of Mg-O are associated with the vibrational bands at 517 cm^{-1} and a peak close to 870 cm^{-1}.[27] Additionally, the peaks at 1320 cm^{-1} and 1127 cm^{-1} correspond to the stretching vibrations of C=O and C-O, respectively.[28]

3.2. Microstructural analyses

Fig. 4 represents the high-resolution scanning electron microscopic (HRSEM) images of MCSZO-X nanoparticles. The average particle size of MCSZO-X nanoparticles increased from 346 to 452 nm as the amount of Ca/Zr in MCSZO-X was raised from 0 to 4.

3.3. Leaching behavior

Fig. 5 illustrates the amounts of Ca^{2+}, Mg^{2+}, Si^{4+}, and Zr^{4+} ions, leached from MCSZO-X nanoparticles after 3, 5, and 7 days of immersion in saline. The leaching of Mg^{2+}, and Si^{4+} ions from different nanoparticles (M1, M2, M3, M4, and M5) are lower in comparison to pure MCSZO-X (X = 0) nanoparticles as the concentration of Mg^{2+} and Si^{4+} decreases with increasing the concentration of Ca^{2+} and Zr^{4+} dopant. However, the leaching of Ca^{2+} and Zr^{4+} ions increase. In addition, the amount of Ca^{2+}, leached from MCSZO-X nanoparticles is also increased with increase in the immersion time.

Bones incorporate ions such as Mg^{2+}, Ca^{2+}, Zr^{4+}, and Si^{4+}, which play vital roles in regulating various metabolic activities, including supporting bone formation and reducing the risk of osteoporosis.[10, 29-32] Ca plays a vital role and also affects the metabolic functions of osteoblast cells.[29, 33] Concentrations of Ca^{2+} ions above 10 mM have been shown to exert cytotoxic effects, whereas levels in the 2–4 mM range support osteoblast proliferation and differentiation, thereby enhancing the osteogenic response.[34] Si is essential for bone development and overall bone health.[10] Incorporating zirconium into Ca–Si-based bioceramics, like baghdadite, has been reported to enhance the attachment and growth of osteoblast-like cells.[35]

View Article Online
DOI: 10.1039/D5LF00045A

3.4. Cell viability

The viability of MG-63 cells was evaluated using MTT assay at different elute concentrations (C1, C2, and C3 for M1, M2, M3, M4 and M5 samples). Fig. 6. demonstrates the proliferation of MG-63 cells on prepared MCSZO-X nanoparticles, after 1 and 3 days of incubation. The viability of osteoblast-like MG-63 cells, cultured on the MCSZO-X nanoparticles, was lower than the control after 1 day.

This is probably due to the physical damage of the cells due to the early stage interaction with nanoparticle eluates. However, after 3 days of culture, the cell viability significantly as compared to those on after 1 day of incubation, across all the concentrations of MCSZO-X nanoparticles. For these samples, the viability was comparable to that of the control group [Fig. 6 (b)].

3.5. *In-vivo* studies

3.5.1. General observation

After injecting the MCSZO-X particles for seven days, the skin texture and salivation of the rat remained unchanged. Also, after the intra-articular injection, the rats did not exhibit symptoms such as diarrhea, tremor, or convulsions. Additionally, after seven days of post-injection, no notable changes were observed in the behavior of rats. Also, the injection site in every group of rats did not display any sign of inflammation (swelling or redness) throughout the observation period. Digital cameras were used to take paw photographs of the rats, treated with MCSZO-X particles injected group, which were then compared to the paw images of the control as well as saline-treated groups [Fig. 7].

The paws of the rats, injected with MCSZO-X nanoparticles (M1, M2, M3, M4 and M5), are similar to those of the saline-treated and control rats, revealing no indication of abnormalities, inflammation, redness, or edema. Likewise, after completion of the experiment, the knee joints of the control, saline and treated rats displayed unchanged morphology.

View Article Online
DOI: 10.1039/D5LF00045A

Furthermore, as aforementioned, no inflammation was detected at the injection site, and no signs of atrophy were noted in the adjacent bone structures such as the tibia and femur. This result corresponds to the *in vitro* cytocompatibility of MCSZO-X nanoparticles with varying concentrations of Ca / Zr [Fig. 6].

3.5.1.1. Impact of intra-articular injection of MCSZO-X on body weight

The variation in body weight is crucial for assessing whether injected nanoparticles have adversely affected the function of vital organs.[36, 37] Consequently, before and after (after 7 days) injection, the weights of each of the 35 rats were recorded. Control, saline, and MCSZO-X nanoparticle injected rats did not show any significant weight changes [Fig. 8]. Statistical analyses using two-way ANOVA showed no noticeable variation in body weight. [38]

3.5.2. Hematological analyses

Changes in hematological parameters in humans and animals are indicative of drug-induced toxicity. The hemotopoietic system is a vital body system that produces the cellular blood components.[38] In this study, the effects of intrarticularly injected MCSZO-X nanoparticles on the blood cells such as, WBC and MCV were evaluated as compared to the control group [Fig. 9]. The evaluation of basic hematological parameters, such as the measurement of WBC and MCV is a crucial stage in the toxicity detection process.

The statistical analyses showed no significant variation in WBC ($p > 0.05$) among all groups in MCSZO-X nanoparticles injected rats in comparison to the saline group [Fig. 9 (a)]. Also, there were no notable changes in the MCV ($p > 0.05$) among all the injected MCSZO-X nanoparticles groups as compared to the saline groups [Fig. 9 (b)].

3.5.3. Biochemical assays

The impact of MCSZO-X nanoparticles (X = 0 - 4) on enzyme levels in rat blood was assessed by analyzing the biochemical properties of the extracted serum.

View Article Online
DOI: 10.1039/D5LF00045A

Typically, the hepatic function is assessed by measuring the serum ALP activity level. The breakdown and restoration of liver tissue contribute to alteration in ALP activity.[39, 40] Additionally, hepatotoxicity raised by chemicals or drugs also increases the ALP activity in blood serum.[41, 42]

As a result, the liver is an essential organ for examining the impact of toxicity induced by the nanoparticles. In this study, MCSZO-X nanoparticles were injected into the synovial joint. ALP, a marker of bone formation, plays an essential role in determining whether MCSZO-X nanoparticle exposure caused any bone abnormalities. The statistical analyses reveal that there were no significant changes in serum levels (ALP) between the control and MCSZO-X nanoparticle treated (M1, M2, M3, M4 and M5) groups [Fig. 10 (a)]. Consequently, exposure to MCSZO-X nanoparticles did not alter liver function. Moreover, the assessment of serum creatinine levels is a typical method to detect potential adverse effects on renal function (Creatinine) caused by implant or foreign particles.[43]

Elevated blood creatinine levels indicate reduced kidney filtration capacity.[44-47] In this study, the creatinine levels in the rat's blood serum, injected with M1, M2, M3, M4 and M4 nanoparticles, do not show any substantial differences in comparison to the saline group [Fig. 10 (b)]. Also, the MCSZO-X nanoparticles did not lead to kidney impairment.

3.5.4. Histopathological analyses

Over the period of seven days, it is possible that the nanoparticles, injected into the intraarticular region can enter the blood circulation and reach to organs like liver, kidney, lung and heart as a result of regular physiological processes. Therefore, the histopathological analyses of the liver, heart, kidney and knee was done to determine the toxicity of MCSZO-X (X= 0 - 4) nanoparticles. The comparison of histological images of various stained organs from particulate-injected groups (M1, M2, M3, M4, M5) with control and saline-injected groups are shown in Figs. 11 - 14.

View Article Online
DOI: 10.1039/D5LF00045A

The sections of all the stained organs, in general, reveal the normal appearance and without the presence of eluate particles. The MCSZO-X treated groups (M1, M2, M3, M4, and M5) did not reflect any sign of tissue shrinkage, cardiac muscle disorder, vacuolization, and bleeding. The muscle fibers appear straight and organized, similar to those in the control group (Fig. 11). The connective tissues of the hearts in the nanoparticle-treated rat groups show normal architecture. In number of studies, it has been observed that exposure to fine concentrated particles can result in irregular beat and, in some cases, cardiac dysfunction.[48-52] The injection of TiO_2 nanoparticles has been shown to swell the endothelial cells of the heart, after 7 days.[8]

In this study, the hearts of the rats in the M1, M2, M3, M4 and M5 eluates treated groups did not exhibit enlarged endothelial cells [Fig.11]. Overall, the cardiac tissues of the rats treated with MCSZO-X (M1, M2, M3, M4 and M5) reveal no histopathological changes. Evidently, the kidney is the main organ of the body to remove foreign nanoparticles.[6] As the kidney removes foreign substances from the body by filtering, it is crucial for the kidney to take part to release of nanoparticles if they reach to the vital organs. Besides, the histopathology analyses of kidney's tissue are crucial for both identifying the nanoparticles and determining that how they may affect the structure and functioning of the kidneys.

The exposure to different nanoparticles like ZnO, Au, and TiO_2 causes pathological alterations in the kidney, including necrosis, dispersed glomeruli, and tubular dilatation.[8, 53-55] However, in comparison to control rat groups, the histopathological images of the kidney sections of rats, injected with MCSZO-X particles (M1, M2, M3, M4 and M5) show unchanged renal tubules within the cortex (absence of any indication of vacuolar degeneration) [Fig. 12].

The kidney sections of rats, treated with control and MCSZO-X groups show normal renal cortex and glomerular cells without tubule dilation. Overall, histology of kidney sections

View Article Online
DOI: 10.1039/D5LF00045A

reveals that the intra-articularly injected MCSZO-X nanoparticles (M1, M2, M3, M4 and M5) have no adverse effect on the kidney.

The liver organs play a main role in detoxifying the body. This means that the foreign particles can move through the circulatory or lymphatic systems and into the liver.[56-58] Cytoplasmic vacuolization disrupts the function of the membrane and can occasionally be a sign of liver injury.[59-61] In this study, there is no evidence of any vacuolization in the cytoplasm of hepatocytes in the livers of the rats, treated with MCSZO-X nanoparticles. As a result, histological features of liver cells, injected with MCSZO-X particles (M1, M2, M3, M4 and M5) revealed no indications of any damage, bleeding, or necrosis near the sinusoids, when compared to those of control and saline rats [Fig. 13].

Overall, the histopathological images of the organs stained with H & E of the M1, M2, M3, M4 and M5 injected nanoparticles reveal normal appearance, comparable to that of the control and saline groups. The major organs of the rats of the nanoparticles treated groups show no evidence of particle dissemination.

The histological images provide a clear indication of the presence of nanoparticles within the fibroadipose tissue surrounding the synovial joint [Fig.14 (a-e)]. Moreover, the absence of macrophage infiltration can be clearly seen [Fig. 14 (c-e)], which suggests the biocompatible nature of the prepared MCSZO-X nanoparticles.[62, 63] Furthermore, the administration of MCSZO-X nanoparticles via intra-articular injection did not lead to any injury to the cartilage or excessive growth of the synovial membrane. The thickening of the synovial membrane, which occurs due to an increased density of cells resulting from the influx of different cell types.[64-66] The histological analyses of the knee joint did not reveal any negative response to the intra-articular administration of MCSZO-X nanoparticles.

The histological analyses of rats treated with MCSZO-X (M1, M2, M3, M4 and M5) nanoparticles show no signs of inflammation at the implantation site of injection (synovial

View Article Online
DOI: 10.1039/D5LF00045A

joint) or in vital organs [Fig. 14]. Moreover, MCSZO-X nanoparticles promote the proliferation of MG-63 cells [Fig. 6]. Overall, MCSZO-X nanoparticles demonstrate *in vitro* cytocompatibility and *in vivo* biocompatibility.

In ceramic based implants the wear debris particles such as, Al_2O_3 and ZrO_2 are typically submicron in size.[67, 68] Earlier studies have reported macrophages engulf submicron-sized particles, which increases the risk of an adverse reaction or inflammation.[7, 69, 70] However, histological images of knee joints treated with MCSZO-X nanoparticles showed no signs of macrophage infiltration (Fig. 14 (c-f)), suggesting that MCSZO-X nanoparticles are biocompatible.

6. Conclusion

In vitro investigations indicate that $Mg_{1-x}Ca_xSi_{1-x}Zr_xO_3$ nanoparticles promote the proliferation of MG-63 cells up to concentrations of 25 mg/ml after initial interfacial interaction. The *in vivo* assessment revealed that the nanoparticles, intraarticularly injected into the rats did not migrate to any of the major organs, including the kidney, heart and liver. In addition, the non-toxicity of $Mg_{1-x}Ca_xSi_{1-x}Zr_xO_3$ nanoparticles has been established by histological analyses of the knee and vital organs of rats, exposed to nanoparticle eluates with concentrations as 0.25, 2.5 and 25 mg/ml. Also, the absence of nanoparticles within the essential organs suggests that they were not transported to any of these organs. The histology of knee tissues of the rats, treated with nanoparticles, reveal the absence of any indications of inflammation. Furthermore, biochemical parameters (ALP and creatinine) revealed that $Mg_{1-x}Ca_xSi_{1-x}Zr_xO_3$ nanoparticles had no toxic effect on functioning of vital organs.

Declaration of Competing Interest

The authors declare no conflicts of interest

Funding Declaration

This research was financially supported by SERB, Government of India.

View Article Online
DOI: 10.1039/D5LF00045A

Acknowledgments

The authors sincerely thank Dr Bitan Naik from the Department of Pathology, Institute of Medical Sciences (IMS), Banaras Hindu University (BHU), Varanasi, for histopathological imaging.

List of Figures

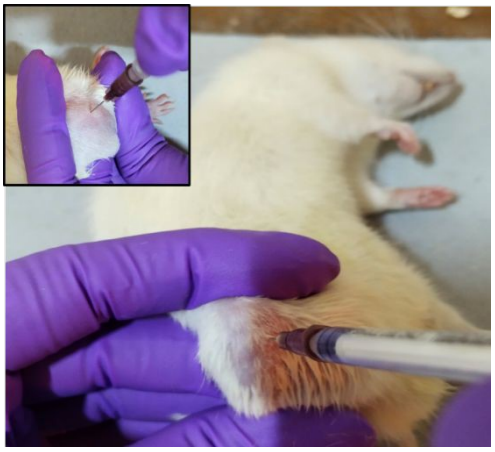

Fig. 1. Representation of intra-articular injection of MCSZO-X (X = 0 – 4) nanoparticles in the Wistar rat knee (synovial) joint.

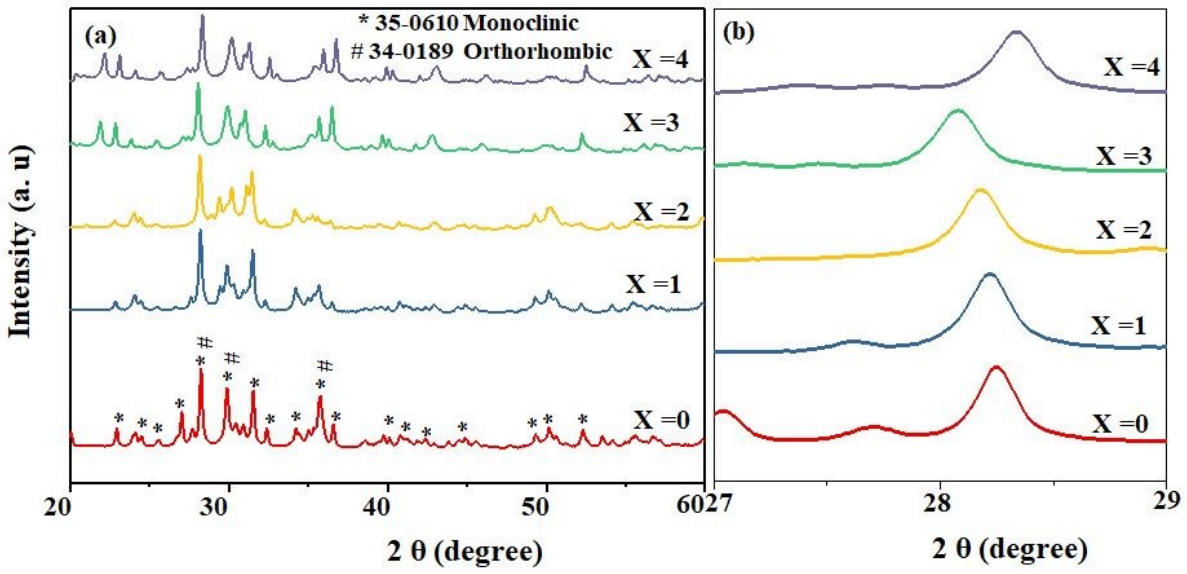

View Article Online
DOI: 10.1039/D5LF00045A

Fig. 2. XRD results of MCSZO-X (X = 0 - 4) nanoparticles. (a) XRD patterns of different samples of MCSZO (X = 0 - 4), calcined at 1300º C for 10 h. (b) enlarged view of the highest intense peaks of samples.

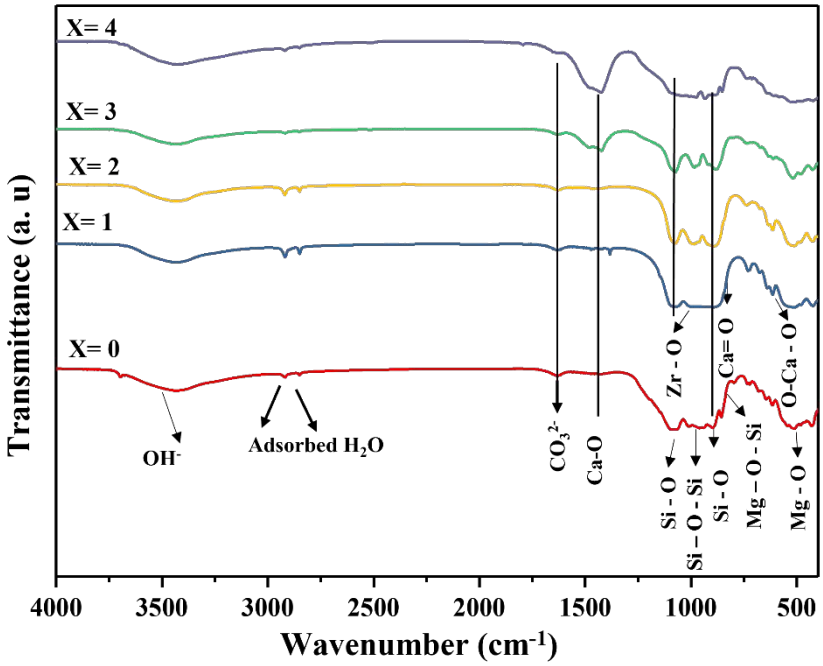

Fig. 3. FT-IR spectra of MCSZO-X (X = 0 - 4) nanoparticles.

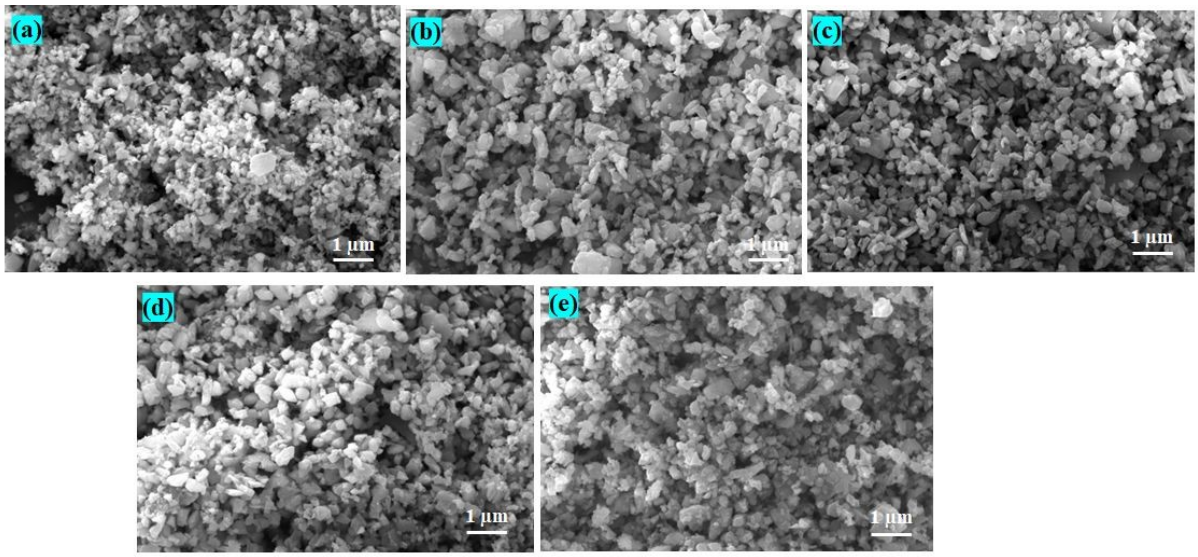

View Article Online
DOI: 10.1039/D5LF00045A

Fig. 4. Scanning electron micrographs of MCSZO-X nanoparticles. (a) X = 0, (b) X = 1, (C) X = 2, (d) X = 3 and (e) X = 4.

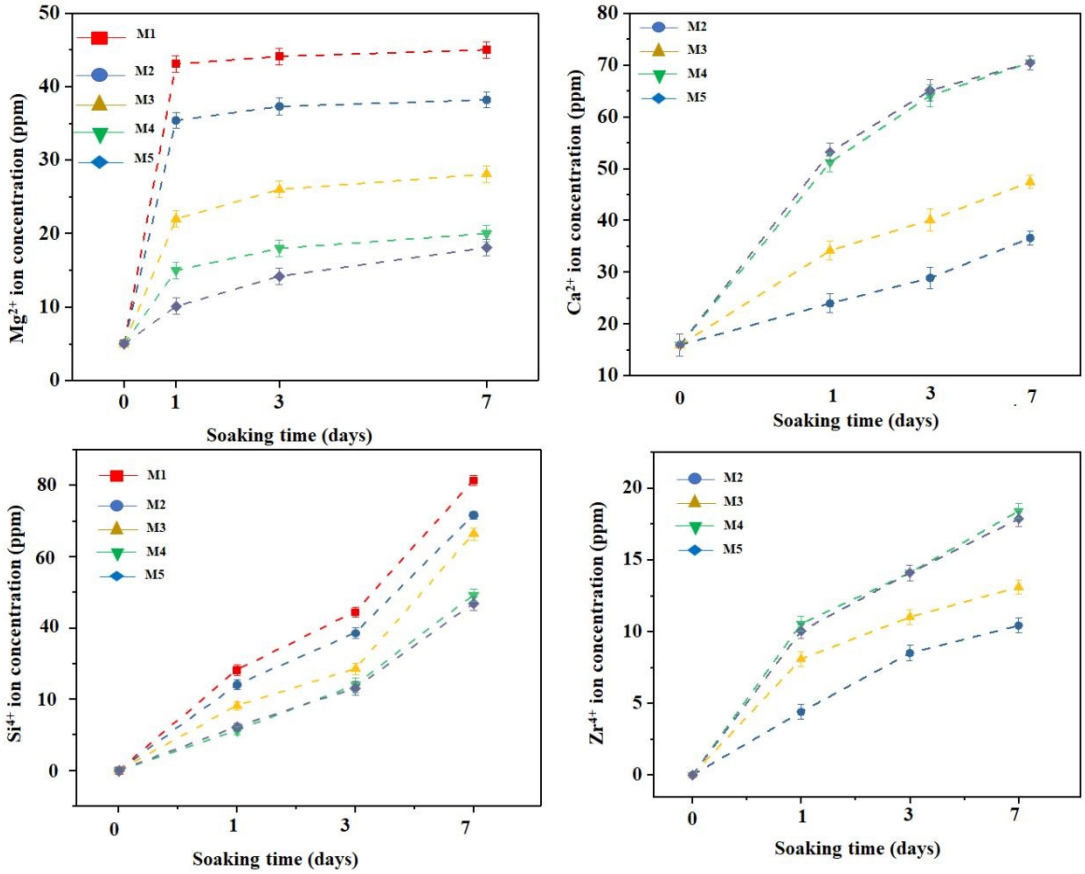

Fig. 5. Leaching behavior of Mg^{2+}, Si^{4+}, Ca^{2+}, and Zr^{4+} ions from MCSZO- X nanoparticles in saline.

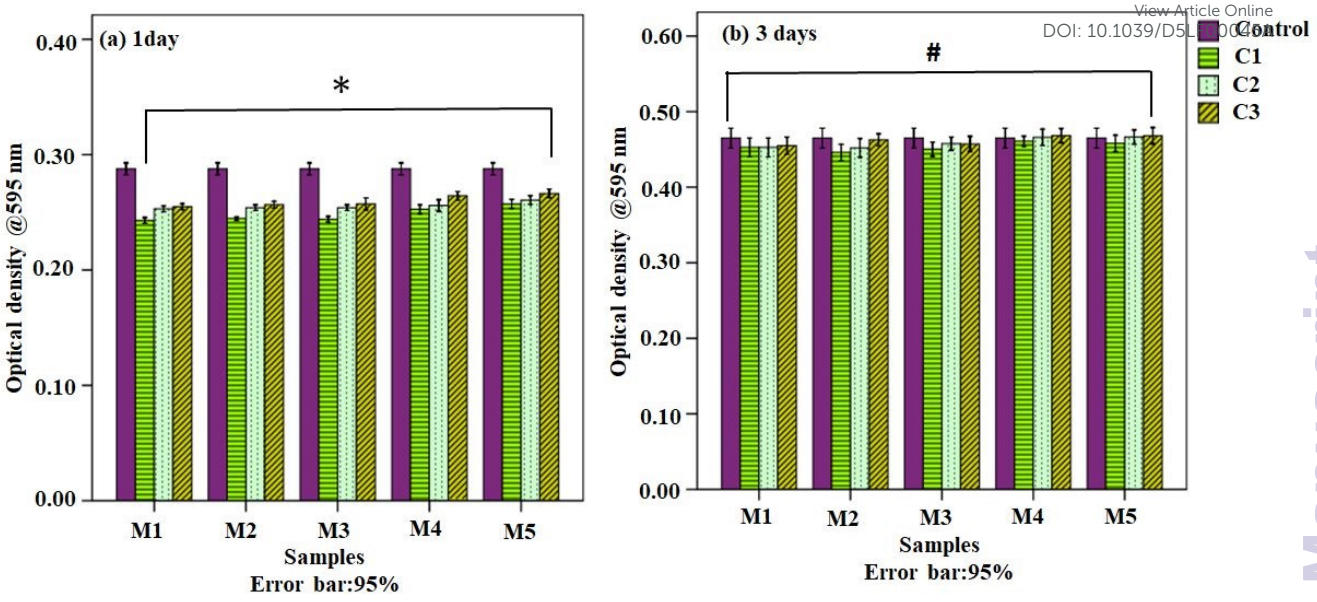

Fig. 6. Optical density of MG-63 cells, after 1 and 3 days of culture, on MCSZO-X (X = 0−4); [M1, M2, M3, M4 and M5) nanoparticles at different concentrations, i.e; 0.25, 2.5 and 25 mg/ml samples] and HA, used as a control. The asterisk symbol (*) indicates the significant variation in optical density across all MCSZO-X samples (M1, M2, M3, M4 and M5) at different concentrations in comparison to control, after 1 day of culture as [Fig. 6 (a)]. However, symbol (#) shows the significant variation in the optical density across all MCSZO-X (M1, M2, M3, M4 and M5) nanoparticles, cultured for 3 days in comparison to the entire MCSZO-X samples, cultured with 1 day [Fig. 6 (b)].

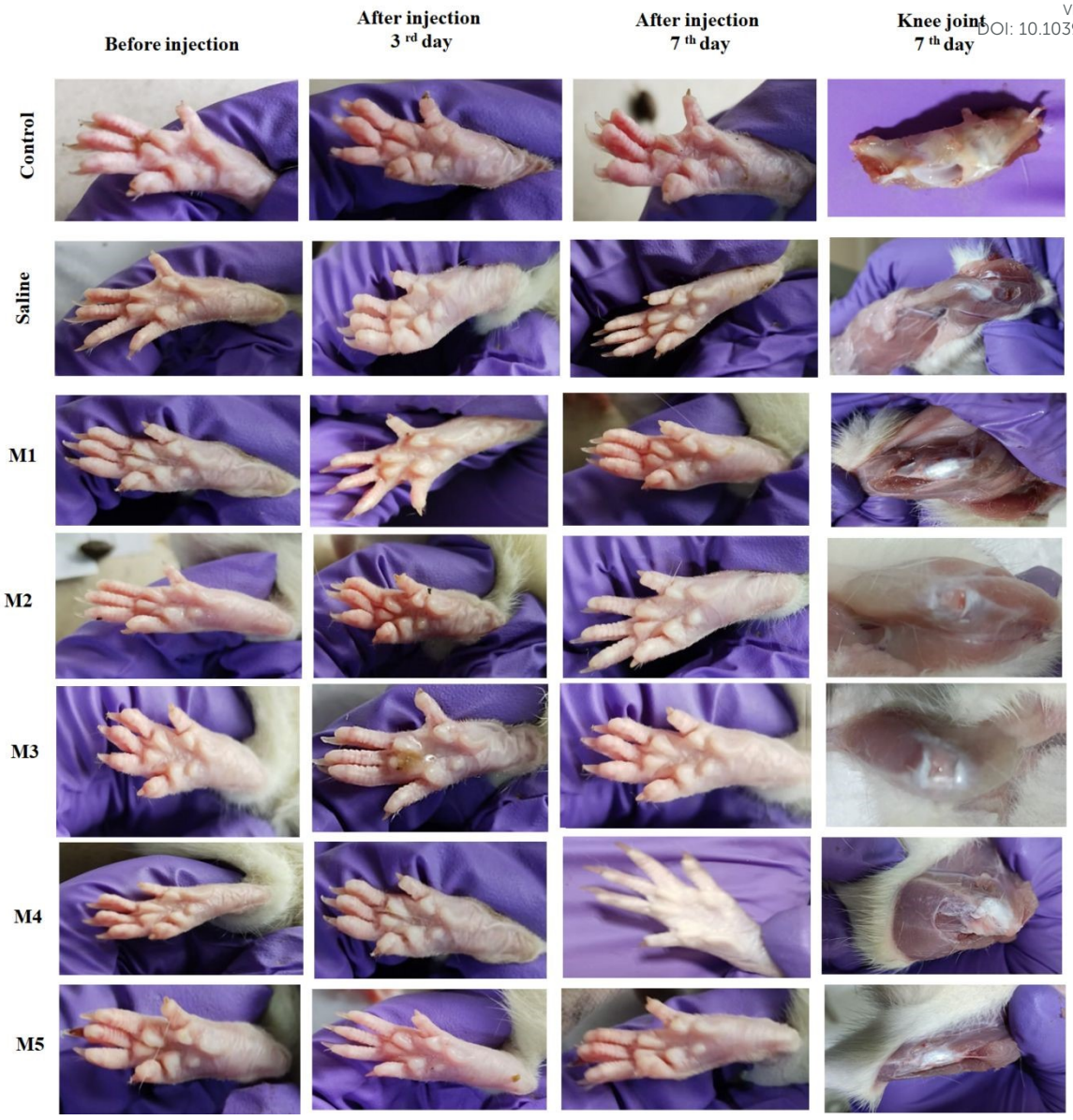

Fig. 7. Digital camera images of rat paws before injection, on the 3rd and 7th day after receiving injections of MCSZO-X nanoparticles into their knee joints.

View Article Online
DOI: 10.1039/D5LF00045A

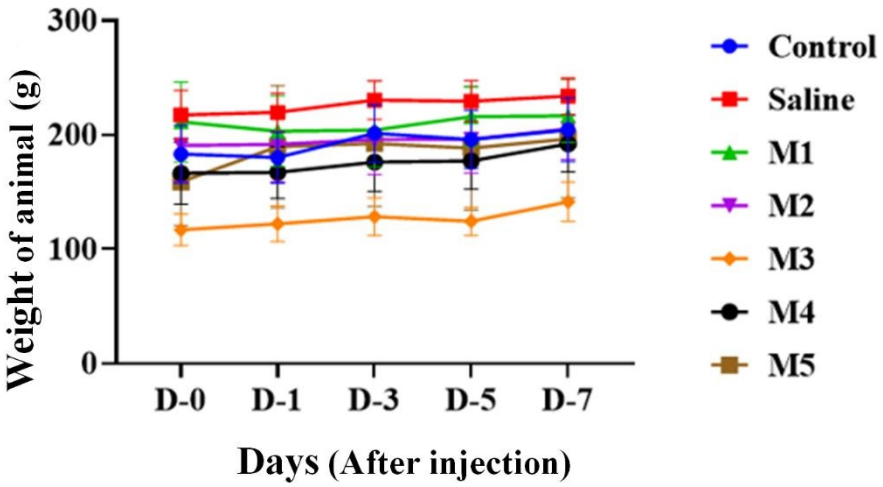

Fig. 8. Effect of intraarticular injection of MCSZO-X (M1, M2, M3, M4 and M5) nanoparticles on the body weight of rat's throughout the experiment. All the results are shown as mean ± standard deviation (n = 5 per group).

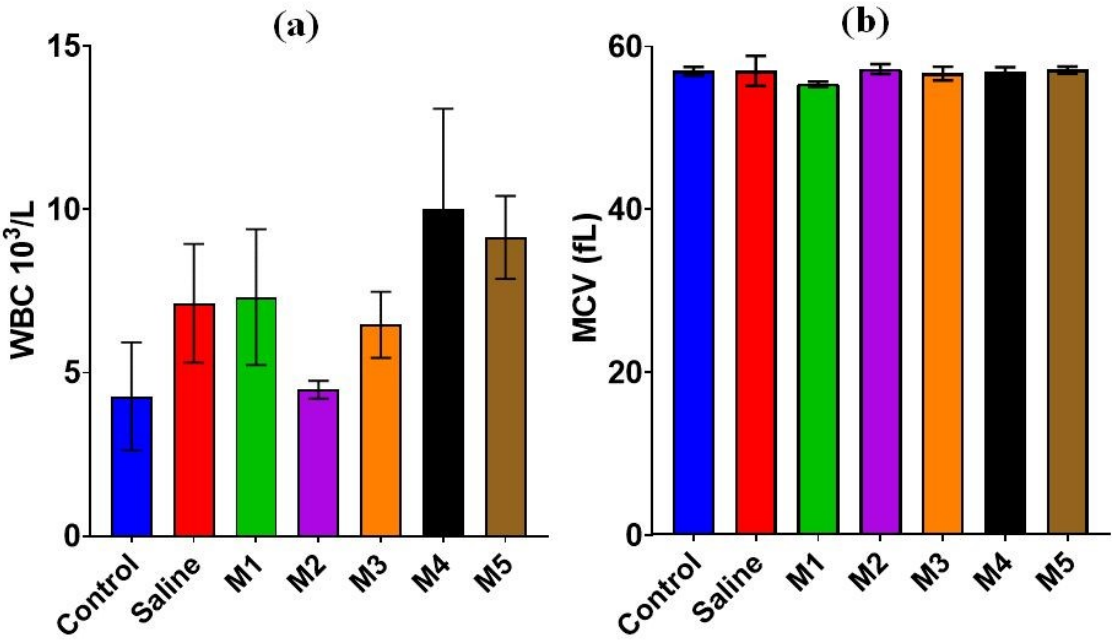

Fig. 9. Effect of intracticular injection of MCSZO-X nanoparticles in rats. (a) WBC count and (b) MCV on 7 days of injection. All the results are shown as mean ± standard deviation (n = 5 per group).

View Article Online
DOI: 10.1039/D5LF00045A

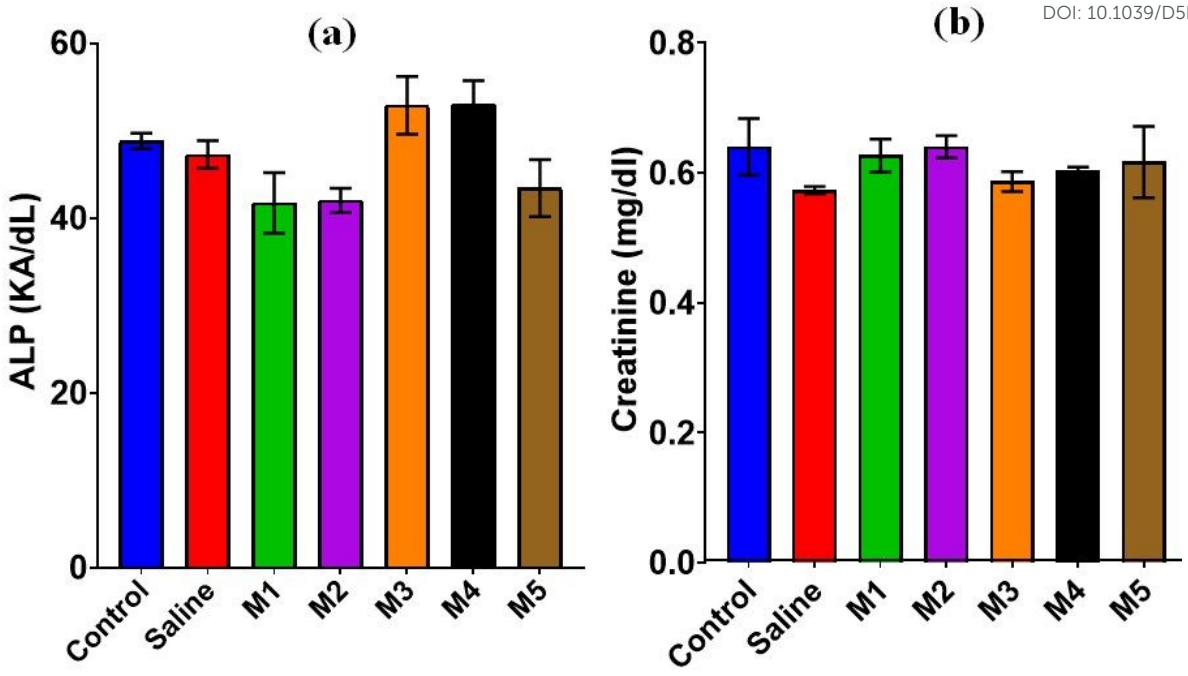

Fig. 10. Effect of MCSZO-X nanoparticles on serum concentration after 7 days of post-injection in rats. (a) ALP and (B) creatinine level. All the results are shown as mean ± standard deviation (n = 5 per group).

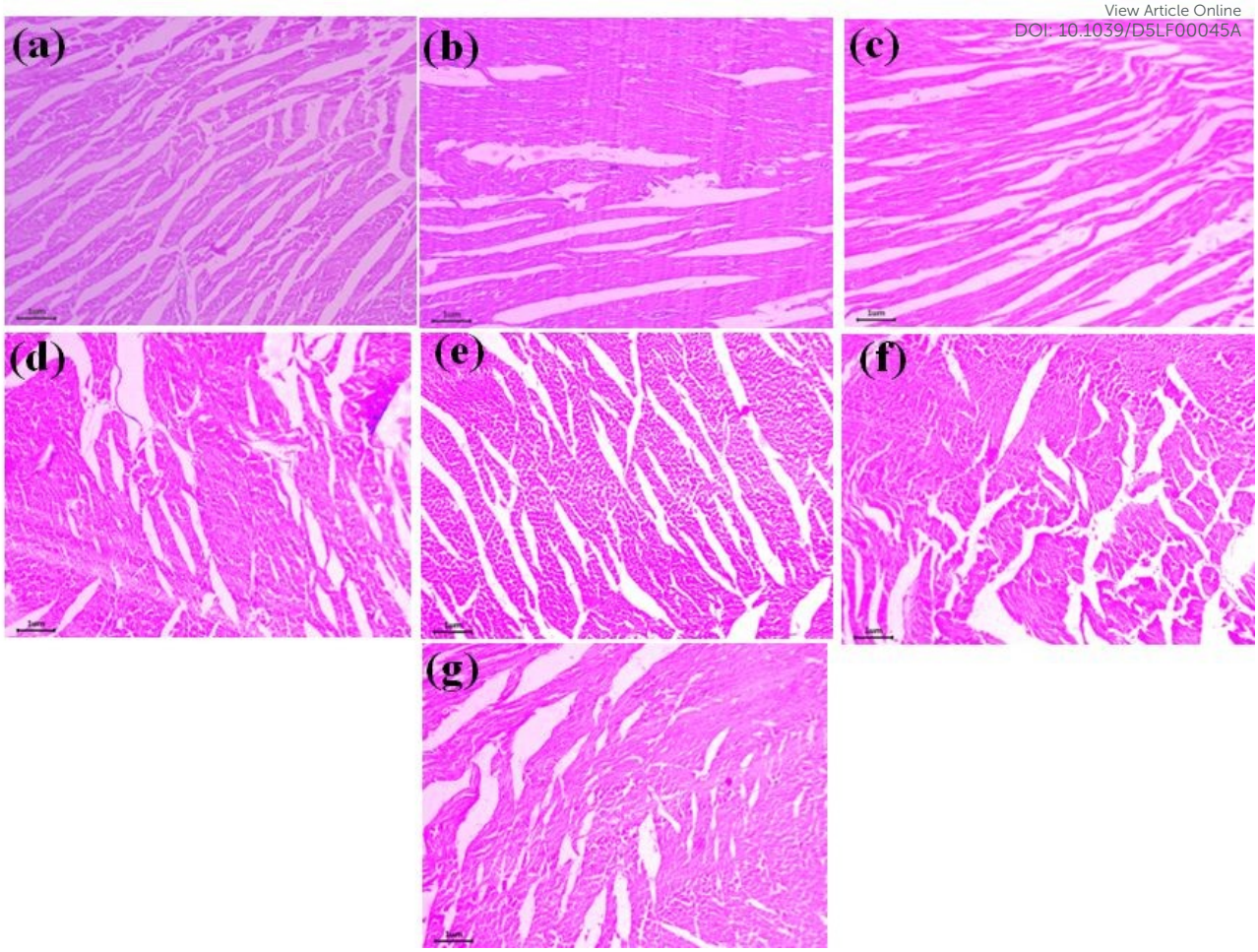

Fig. 11. Histopathological images of the heart tissues, stained with H & E after 7 days of injection in the following groups of rats: (a) Control (non-injected), (b) Saline, (c) M1, (d) M2, (e) M3, (f) M4 and (g) M5 nanoparticles eluates treated groups (Scale bar: 1 μm)

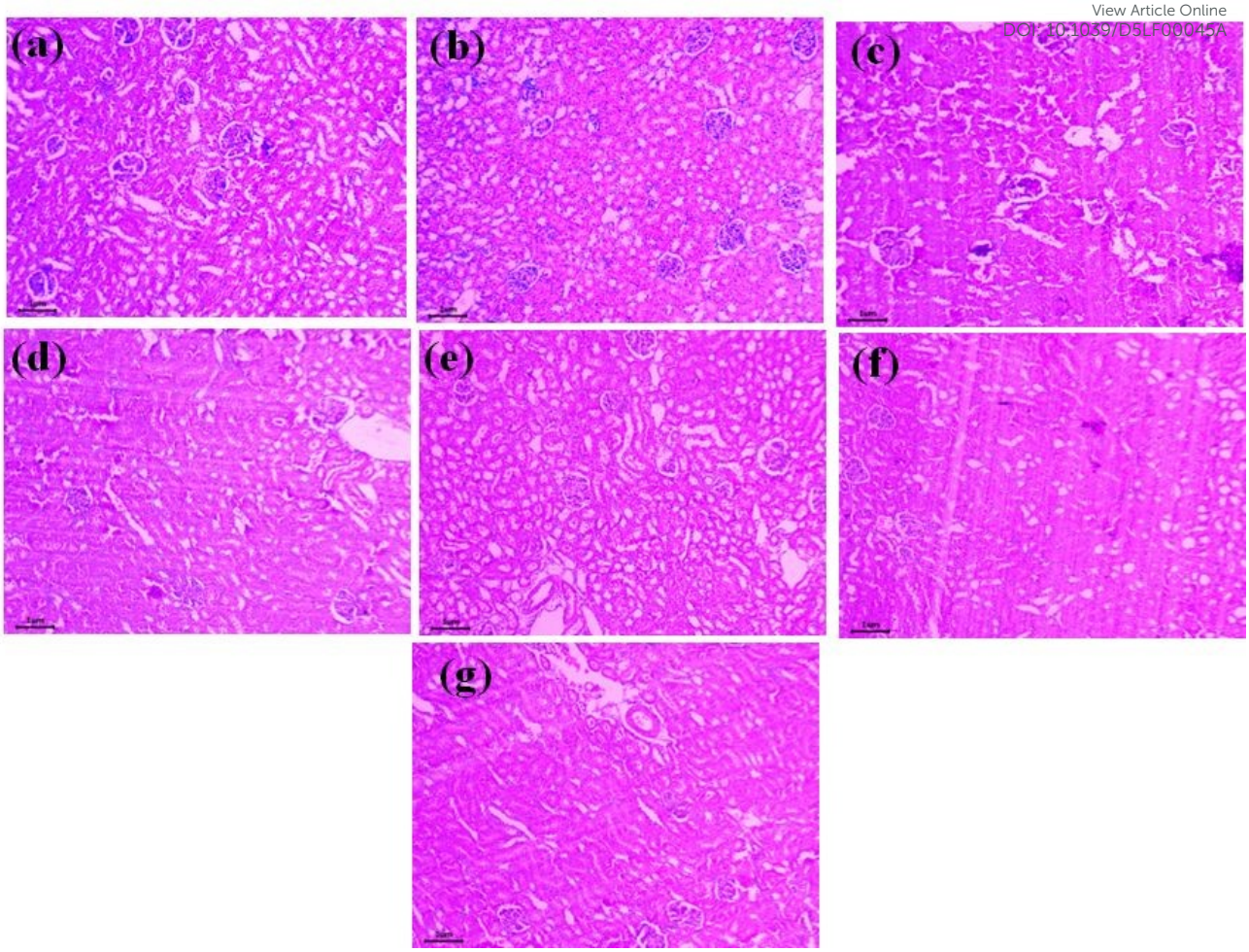

Fig. 12. Histopathological images of the kidney tissues, stained with H & E after 7 days of injection in the following groups of rats: (a) Control (non-injected), (b) Saline, (c) M1, (d) M2, (e) M3, (f) M4 and (g) M5 nanoparticles eluates treated groups (Scale bar: 1 μm)

View Article Online
DOI: 10.1039/D5LF00045A

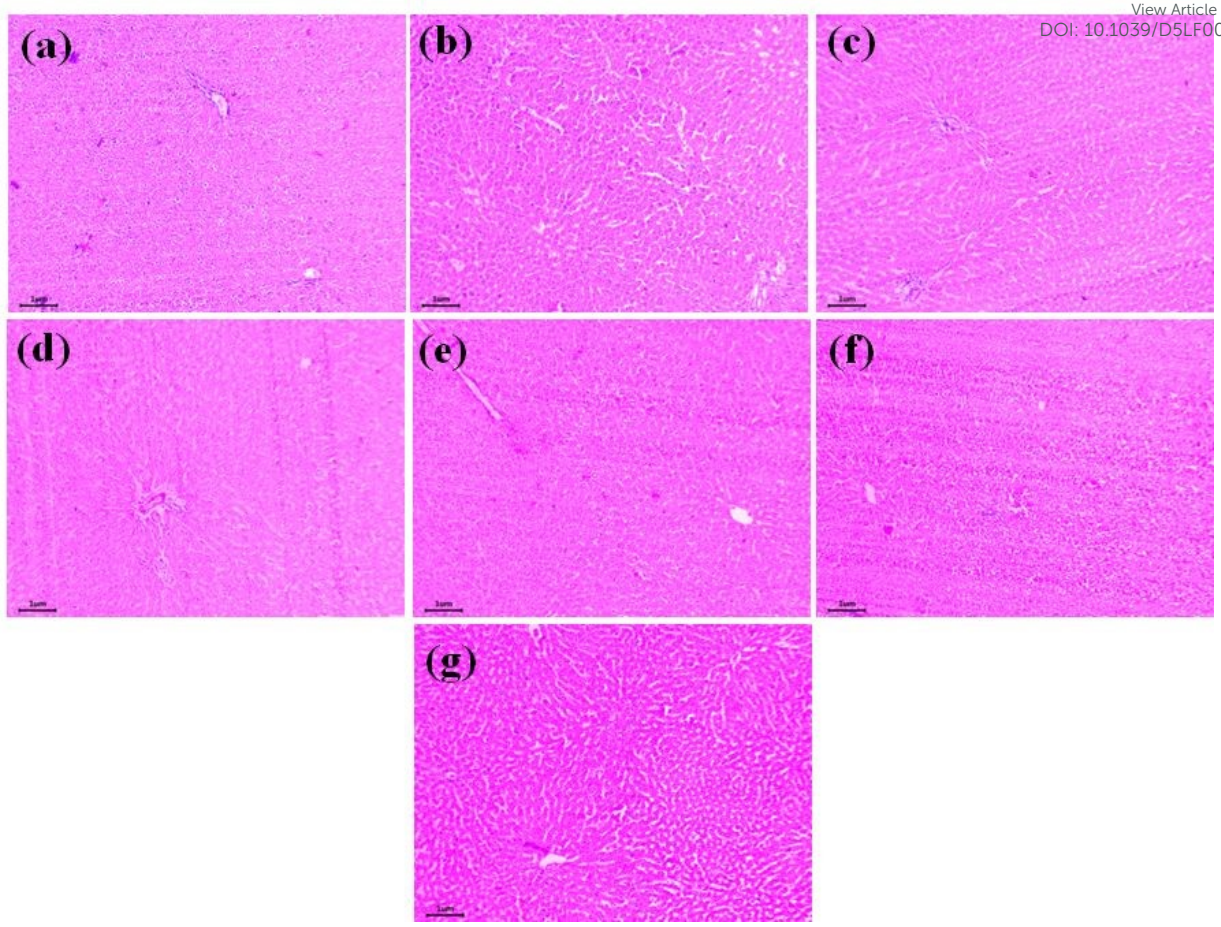

Fig. 13. Histopathological images of the liver section, stained with H & E after 7 days of injection in the following groups of rats: (a) Control (non-injected), (b) Saline, (c) M1, (d) M2, (e) M3, (f) M4 and (g) M5 nanoparticles eluates treated groups (Scale bar: 1 μm)**.**

View Article Online
DOI: 10.1039/D5LF00045A

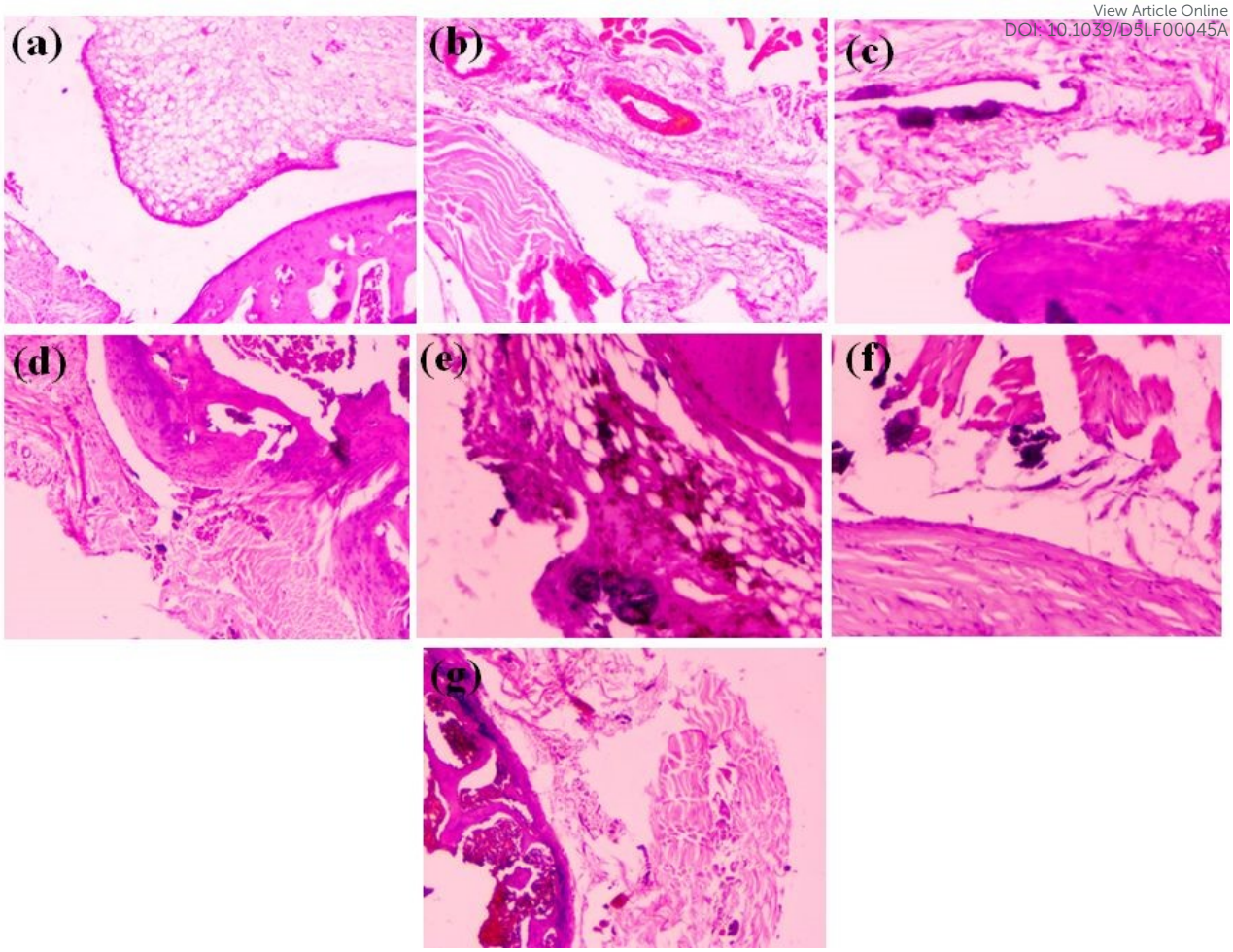

Fig. 14. Histopathological features of rat knee joint tissue, stained with H & E of intra-articular injection after 7 days in the following groups of rats: (a) Control (non-injected), (b) Saline, (c) M1, (d) M2, (e) M3, (f) M4 and (g) M5 nanoparticles eluates treated groups (Scale bar: 1 μm)**.**

View Article Online
DOI: 10.1039/D5LF00045A

References

1. Zhang L, Haddouti E-M, Welle K, Burger C, Wirtz DC, Schildberg FA, et al. The effects of biomaterial implant wear debris on osteoblasts. Frontiers in cell and developmental biology. 2020;8:352.

2. Hu CY, Yoon T-R. Recent updates for biomaterials used in total hip arthroplasty. Biomaterials research. 2018;22(1):1-12.

3. Learmonth ID, Young C, Rorabeck C. The operation of the century: total hip replacement. The Lancet. 2007;370(9597):1508-19.

4. Stratton-Powell AA, Pasko KM, Brockett CL, Tipper JL. The biologic response to polyetheretherketone (PEEK) wear particles in total joint replacement: a systematic review. Clinical Orthopaedics and Related Research®. 2016;474(11):2394-404.

5. Chen Z, Meng H, Xing G, Chen C, Zhao Y, Jia G, et al. Acute toxicological effects of copper nanoparticles in vivo. Toxicology letters. 2006;163(2):109-20.

6. Ding T, Xue Y, Lu H, Huang Z, Sun J. Effect of particle size of hydroxyapatite nanoparticles on its biocompatibility. IEEE Transactions on Nanobioscience. 2012;11(4):336-40.

7. Margevicius KJ, Bauer TW, McMahon JT, Brown SA, Merritt K. Isolation and characterization of debris in membranes around total joint prostheses. JBJS. 1994;76(11):1664-75.

8. Wang J-X, Fan Y-B, Gao Y, Hu Q-H, Wang T-C. TiO2 nanoparticles translocation and potential toxicological effect in rats after intraarticular injection. Biomaterials. 2009;30(27):4590-600.

9. Mabrouk M, Ibrahim Fouad G, Beherei HH, Das DB. Barium Oxide Doped Magnesium Silicate Nanopowders for Bone Fracture Healing: Preparation, Characterization, Antibacterial and In Vivo Animal Studies. Pharmaceutics. 2022;14(8):1582.

10. Singh P, Yu X, Kumar A, Dubey AK. Recent advances in silicate-based crystalline bioceramics for orthopedic applications: a review. Journal of Materials Science. 2022;57(28):13109-51.

11. Singh P, Dubey AK. Accelerated Osteogenic Response of Electrodynamically Stimulated Mg1–xCaxSi1–xZrxO3 (x = 0–0.4) Bioelectrets. ACS Biomaterials Science & Engineering. 2023;9(11):6293-308.

12. Singh P, Dubey AK. Electret-induced antibacterial response of Mg1-xCaxSi1-xZrxO3 (x= 0–0.4) bioceramics. Journal of the American Ceramic Society. 2024.

13. Venkatraman SK, Swamiappan S. Review on calcium-and magnesium-based silicates for bone tissue engineering applications. Journal of Biomedical Materials Research Part A. 2020;108(7):1546-62.

14. Bavya Devi K, Nandi SK, Roy M. Magnesium Silicate Bioceramics for Bone Regeneration: A Review. Journal of the Indian Institute of Science. 2019;99(3):261-88.

View Article Online
DOI: 10.1039/D5LF00045A

15. Ni S, Chang J. In vitro degradation, bioactivity, and cytocompatibility of calcium silicate, dimagnesium silicate, and tricalcium phosphate bioceramics. Journal of biomaterials applications. 2009;24(2):139-58.

16. Bakhsheshi-Rad H, Najafinezhad A, Hadisi Z, Iqbal N, Daroonparvar M, Sharif S, et al. Characterization and biological properties of nanostructured clinoenstatite scaffolds for bone tissue engineering applications. Materials Chemistry and Physics. 2021;259:123969.

17. Shin J-H, Lee D-Y, Lee S-H. Comparison of antimicrobial activity of traditional and new developed root sealers against pathogens related root canal. Journal of Dental Sciences. 2018;13(1):54-9.

18. Singh P, Dubey AK. Accelerated Osteogenic Response of Electrodynamically Stimulated Mg1–x Ca x Si1–x Zr x O3 (x= 0–0.4) Bioelectrets. ACS Biomaterials Science & Engineering. 2023;9(11):6293-308.

19. Cullity BD. Elements of X-ray Diffraction: Addison-Wesley Publishing; 1956.

20. Londoño-Restrepo SM, Jeronimo-Cruz R, Millán-Malo BM, Rivera-Muñoz EM, Rodriguez-García ME. Effect of the nano crystal size on the X-ray diffraction patterns of biogenic hydroxyapatite from human, bovine, and porcine bones. Scientific reports. 2019;9(1):5915.

21. Parthasarathy S, Parthasarathi V. A statistical study on the measurability of Bijvoet differences in crystals with type-I and type-II degree of centrosymmetry. Acta Crystallographica Section A: Crystal Physics, Diffraction, Theoretical and General Crystallography. 1976;32(5):768-71.

22. Shannon RD. Revised effective ionic radii and systematic studies of interatomic distances in halides and chalcogenides. Foundations of Crystallography. 1976;32(5):751-67.

23. Sun H, Zhang Q, Yang H, Zou J. (Ca1− xMgx) SiO3: a low-permittivity microwave dielectric ceramic system. Materials Science and Engineering: B. 2007;138(1):46-50.

24. Smyth JR. Experimental study on the polymorphism of enstatite. American Mineralogist: Journal of Earth and Planetary Materials. 1974;59(3-4):345-52.

25. Choi CK. Comparison between SiOC Thin Film by plasma enhance chemical vapor deposition and SiO2 Thin Film by Fourier Transform Infrared Spectroscopy? Journal of the Korean Physical Society. 2010;56(4):1150-5.

26. Vancea C, Mihailescu M, Negrea A, Mosoarca G, Ciopec M, Duteanu N, et al. Batch and fixed-bed column studies on palladium recovery from acidic solution by modified MgSiO3. International Journal of Environmental Research and Public Health. 2020;17(24):9500.

27. Sagadevan S, Venilla S, Marlinda A, Johan M, Wahab YA, Zakaria R, et al. Effect of synthesis temperature on the morphologies, optical and electrical properties of MgO nanostructures. Journal of nanoscience and nanotechnology. 2020;20(4):2488-94.

View Article Online
DOI: 10.1039/D5LF00045A

28. Kumar P, Dehiya BS, Sindhu A, Kumar R, Pruncu CI, Yadav A. Fabrication and characterization of silver nanorods incorporated calcium silicate scaffold using polymeric sponge replica technique. Materials & Design. 2020;195:109026.

29. Dufrane D, Delloye C, Mckay I, De Aza P, De Aza S, Schneider Y-J, et al. Indirect cytotoxicity evaluation of pseudowollastonite. Journal of Materials Science: Materials in Medicine. 2003;14:33-8.

30. Schwarz K. A bound form of silicon in glycosaminoglycans and polyuronides. Proceedings of the National Academy of Sciences. 1973;70(5):1608-12.

31. Mohammadi H, Hafezi M, Nezafati N, Heasarki S, Nadernezhad A, Ghazanfari S, et al. Bioinorganics in bioactive calcium silicate ceramics for bone tissue repair: bioactivity and biological properties. J Ceram Sci Technol. 2014;5(1):1-12.

32. Pravina P, Sayaji D, Avinash M. Calcium and its role in human body. International Journal of Research in Pharmaceutical and Biomedical Sciences. 2013;4(2):659-68.

33. Wu C, Chang J, Wang J, Ni S, Zhai W. Preparation and characteristics of a calcium magnesium silicate (bredigite) bioactive ceramic. Biomaterials. 2005;26(16):2925-31.

34. Maeno S, Niki Y, Matsumoto H, Morioka H, Yatabe T, Funayama A, et al. The effect of calcium ion concentration on osteoblast viability, proliferation and differentiation in monolayer and 3D culture. Biomaterials. 2005;26(23):4847-55.

35. Ramaswamy Y, Wu C, Van Hummel A, Combes V, Grau G, Zreiqat H. The responses of osteoblasts, osteoclasts and endothelial cells to zirconium modified calcium-silicate-based ceramic. Biomaterials. 2008;29(33):4392-402.

36. El Hilaly J, Israili ZH, Lyoussi B. Acute and chronic toxicological studies of Ajuga iva in experimental animals. Journal of ethnopharmacology. 2004;91(1):43-50.

37. Bailey SA, Zidell RH, Perry RW. Relationships between organ weight and body/brain weight in the rat: what is the best analytical endpoint? Toxicologic pathology. 2004;32(4):448-66.

38. Buesen R, Landsiedel R, Sauer UG, Wohlleben W, Groeters S, Strauss V, et al. Effects of SiO 2, ZrO 2, and BaSO 4 nanomaterials with or without surface functionalization upon 28-day oral exposure to rats. Archives of toxicology. 2014;88:1881-906.

39. Kaplan MM, Righetti A. Induction of rat liver alkaline phosphatase: the mechanism of the serum elevation in bile duct obstruction. The Journal of clinical investigation. 1970;49(3):508-16.

40. Gawlik Z, Fiejka E, Aleksandrowicz R, Wiśniewska I. Activity of alkaline phosphatase in the healing rat liver after hepatectomy. Folia Histochemica et Cytochemica. 1978;16(4):343-9.

41. Wright TM, Vandenberg AM. Risperidone-and quetiapine-induced cholestasis. Annals of Pharmacotherapy. 2007;41(9):1518-23.

42. Singh A, Bhat T, Sharma O. Clinical biochemistry of hepatotoxicity. J Clinic Toxicol S. 2011;4:2161-0495.

View Article Online
DOI: 10.1039/D5LF00045A

43. Panda N. Kidney in: Textbook of Biochemistry and Human biology. Prentise Hall India. 1999:290-6.

44. Chan P, O'hara G, Hayes AW. Principles and methods for acute and subchronic toxicity. Principles and methods of toxicology. 1982;12:17-9.

45. Adefemi O, Elujoba A, Odesanmi W. Evaluation of the toxicity potential of Cassia podocarpa with reference to official Senna. West Afr J Pharmacol Drug Res. 1988;8:41-8.

46. Oh RC, Hustead TR. Causes and evaluation of mildly elevated liver transaminase levels. American family physician. 2011;84(9):1003-8.

47. Ene-ojo AS, Chinedu EA, Yakasai FM. Toxic Effects of Sub-Chronic Administration of Chloroform Extract of Artemisia maciverae Linn on the Kidney of Swiss Albino Rats. 2013.

48. Timonen KL, Vanninen E, De Hartog J, Ibald-Mulli A, Brunekreef B, Gold DR, et al. Effects of ultrafine and fine particulate and gaseous air pollution on cardiac autonomic control in subjects with coronary artery disease: the ULTRA study. Journal of exposure science & environmental epidemiology. 2006;16(4):332-41.

49. Rich DQ, Zareba W, Beckett W, Hopke PK, Oakes D, Frampton MW, et al. Are ambient ultrafine, accumulation mode, and fine particles associated with adverse cardiac responses in patients undergoing cardiac rehabilitation? Environmental health perspectives. 2012;120(8):1162-9.

50. Peters A, Hampel R, Cyrys J, Breitner S, Geruschkat U, Kraus U, et al. Elevated particle number concentrations induce immediate changes in heart rate variability: a panel study in individuals with impaired glucose metabolism or diabetes. Particle and fibre toxicology. 2015;12(1):1-11.

51. Brook RD, Brook JR, Urch B, Vincent R, Rajagopalan S, Silverman F. Inhalation of fine particulate air pollution and ozone causes acute arterial vasoconstriction in healthy adults. Circulation. 2002;105(13):1534-6.

52. Hamanaka RB, Mutlu GM. Particulate matter air pollution: effects on the cardiovascular system. Frontiers in endocrinology. 2018;9:680.

53. Ibrahim KE, Al-Mutary MG, Bakhiet AO, Khan HA. Histopathology of the liver, kidney, and spleen of mice exposed to gold nanoparticles. Molecules. 2018;23(8):1848.

54. Yan G, Huang Y, Bu Q, Lv L, Deng P, Zhou J, et al. Zinc oxide nanoparticles cause nephrotoxicity and kidney metabolism alterations in rats. Journal of Environmental Science and Health, Part A. 2012;47(4):577-88.

55. Noori A, Karimi F, Fatahian S, Yazdani F. Effects of zinc oxide nanoparticles on renal function in mice. International Journal of Biosciences (IJB). 2014;5(9):140-6.

56. Lipka J, Semmler-Behnke M, Sperling RA, Wenk A, Takenaka S, Schleh C, et al. Biodistribution of PEG-modified gold nanoparticles following intratracheal instillation and intravenous injection. Biomaterials. 2010;31(25):6574-81.

57. Husain M, Wu D, Saber AT, Decan N, Jacobsen NR, Williams A, et al. Intratracheally instilled titanium dioxide nanoparticles translocate to heart and liver and activate complement cascade in the heart of C57BL/6 mice. Nanotoxicology. 2015;9(8):1013-22.

58. Modrzynska J, Mortensen A, Berthing T, Ravn-Haren G, Szarek J, Saber AT, et al. Effect on mouse liver morphology of CeO2, TiO2 and carbon black nanoparticles translocated from lungs or deposited intravenously. Applied Nano. 2021;2(3):222-41.

59. Abdelhalim MAK, Jarrar BM. Gold nanoparticles administration induced prominent inflammatory, central vein intima disruption, fatty change and Kupffer cells hyperplasia. Lipids in health and disease. 2011;10:1-6.

60. Abdelhalim MAK, Jarrar BM. Gold nanoparticles induced cloudy swelling to hydropic degeneration, cytoplasmic hyaline vacuolation, polymorphism, binucleation, karyopyknosis, karyolysis, karyorrhexis and necrosis in the liver. Lipids in Health and Disease. 2011;10:1-6.

61. Abdelhalim MAK. Gold nanoparticles administration induces disarray of heart muscle, hemorrhagic, chronic inflammatory cells infiltrated by small lymphocytes, cytoplasmic vacuolization and congested and dilated blood vessels. Lipids in health and disease. 2011;10(1):1-9.

62. Sheikh Z, Brooks PJ, Barzilay O, Fine N, Glogauer M. Macrophages, foreign body giant cells and their response to implantable biomaterials. Materials. 2015;8(9):5671-701.

63. Xia Z, Triffitt JT. A review on macrophage responses to biomaterials. Biomedical materials. 2006;1(1):R1.

64. Sergijenko A, Roelofs AJ, Riemen AH, De Bari C. Bone marrow contribution to synovial hyperplasia following joint surface injury. Arthritis Research & Therapy. 2016;18:1-11.

65. Asif Amin M, Fox DA, Ruth JH, editors. Synovial cellular and molecular markers in rheumatoid arthritis. Seminars in immunopathology; 2017: Springer.

66. Burke CJ, Alizai H, Beltran LS, Regatte RR. MRI of synovitis and joint fluid. Journal of Magnetic Resonance Imaging. 2019;49(6):1512-27.

67. Lerouge S, Huk O, Yahia LH, Sedel L. Characterization of in vivo wear debris from ceramic—ceramic total hip arthroplasties. Journal of Biomedical Materials Research: An Official Journal of The Society for Biomaterials and The Japanese Society for Biomaterials. 1996;32(4):627-33.

68. Hatton A, Nevelos J, Nevelos A, Banks R, Fisher J, Ingham E. Alumina–alumina artificial hip joints. Part I: a histological analysis and characterisation of wear debris by laser capture microdissection of tissues retrieved at revision. Biomaterials. 2002;23(16):3429-40.

69. Yang S-Y, Ren W, Park Y, Sieving A, Hsu S, Nasser S, et al. Diverse cellular and apoptotic responses to variant shapes of UHMWPE particles in a murine model of inflammation. Biomaterials. 2002;23(17):3535-43.

70. Thrivikraman G, Madras G, Basu B. In vitro/in vivo assessment and mechanisms of toxicity of bioceramic materials and its wear particulates. RSC Advances. 2014;4(25):12763-81.

View Article Online
DOI: 10.1039/D5LF00045A

Data availability statement

In the manuscript entitled "***Interfacial response of Mg-Ca-Si-Zr Nanoparticles for Transformative Orthopedic Therapeutics***", authored by **Priya Singh**, **Somesh Agrawal, Deepak Khare, Vinod Tiwari and Ashutosh Kumar Dubey,**

The data will be made available on request.

The authors declare no conflict of interest.